ACS APPLIED MATERIALS & INTERFACES

www.acsami.org

Research Article

Wetting Ridge Growth Dynamics on Textured Lubricant-Infused Surfaces

Haobo Xu,[§] Tomasz Kulakowski,[§] Young Jin Lee, and Solomon Adera*

Cite This: *ACS Appl. Mater. Interfaces* 2025, 17, 31677−31684

Read Online

ACCESS | Metrics & More | Article Recommendations | Supporting Information

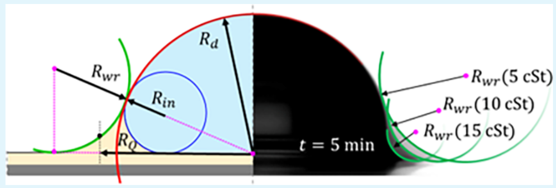

ABSTRACT: Understanding droplet−surface interactions has broad implications in microfluidics and lab-on-a-chip devices. In contrast to droplets on conventional textured air-filled superhydrophobic surfaces, water droplets on state-of-the-art lubricant-infused surfaces are accompanied by an axisymmetric annular wetting ridge, the source and nature of which are not clearly established to date. Generally, the imbalance of interfacial forces at the contact line is believed to play a pivotal role in accumulating the lubricant oil near the droplet base to form the axisymmetric wetting ridge. In this study, we experimentally characterize and model the wetting ridge that plays a crucial role in droplet mobility. We developed a geometry-based analytical model of the steady-state wetting ridge shape that is validated by using experiments and numerical simulations. Our wetting ridge model shows that at steady state (1) the radius of the wetting ridge is ≈30% higher than the droplet radius, (2) the wetting ridge rises halfway to the droplet radius, (3) the volume of the wetting ridge is half (≈50%) of the droplet volume, and (4) the wetting ridge shape does not depend on the oil viscosity used for impregnation. The insights gained from this work improve our state-of-the-art mechanistic understanding of the wetting ridge dynamics.

KEYWORDS: *lubricant-infused surfaces, wetting ridge, fluid-structure interactions, lubricant depletion, three-phase contact line, contact line pinning, wrapping layer*

1. INTRODUCTION

Surface engineering has been used as a tool to effectively manipulate interfacial forces to bring forth enhancements in condensation,[1−5] boiling,[6−8] evaporation,[9−11] water harvesting,[12−14] drag reduction,[15] and numerous other engineering processes.[16,17] Despite sustained efforts over the years, achieving certain combinations of surface properties, some of which seemed contradictory,[18−21] has been challenging both for industry and the scientific community. Nature, having overcome numerous constraints through evolutionary processes, continues to serve as an inspiration for researchers seeking to replicate its sophisticated, yet simple, material design and surface morphology.[22] A prime example of this is in full display with the *Nepenthes* pitcher plant, which coats its leaves with a thin film of water (only few nanometers thick) to inhibit the attachment of insects on its surface.[23−26] Consequently, the oily feet of the insects are vigorously repelled by the ultrathin water film, forcing them to slide down the digestive track of these evolutionary-optimized carnivorous plants.[27] Inspired by *Nepenthes* pitcher plant, micro- and nano-textured surfaces impregnated with lubricant oil have been reported recently.[28−30] These new class of surfaces, which have utility in numerous engineering processes, are commonly referred to as slippery liquid-infused porous surfaces (SLIPS) or lubricant-impregnated surfaces (LIS).[28−32] Water droplets on these surfaces are nearly hemispherical and exhibit exceptionally low contact angle hysteresis (CAH)[33−35] and ultralow drop friction.[36,37] Furthermore, water droplets on these textured oil-impregnated surfaces give rise to some new features that are unique to these surfaces. Example of this is the wetting ridge and wrapping layer, which are absent in traditional nonwetting surfaces. The skirt-like wetting ridge that instantaneously forms when water droplets are deposited on lubricant-infused surfaces is not fully understood to date.[38−44] There is no consensus on the growth dynamics and influence of the wetting ridge on droplet motion despite numerous experimental[43] and analytical[44] investigations. Schellenberger et al.[43] experimentally studied the influence of the wetting ridge on the apparent, advancing, and receding contact angles of droplets on these hemi-solid hemi-liquid surfaces. Similarly, numerical studies of droplet motion over microstructures infused with oil[44] revealed that this phenomenon needs to be analyzed by accounting for both adhesion forces and viscous friction. Dai and Vella[42] conducted a rigorous theoretical analysis of forces acting on a sessile droplet residing on a lubricant-infused surface. The time-dependent equations presented in this work led to an exhaustive

Received: November 19, 2024
Revised: April 7, 2025
Accepted: April 23, 2025
Published: May 8, 2025

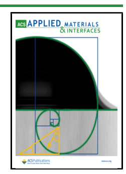

consideration of various aspects affecting growth, such as the thickness of the oil layer, the time to reach steady-state shape, and the distance to neighboring droplets. The analytical results showed that the time-dependent behavior of the wetting ridge growth is complex and depends on many parameters, including interfacial forces, oil viscosity, and droplet size. None of these studies, however, experimentally characterized wetting ridge growth dynamics. Neither are the numerical models easy to use and/or validate.

In this work, not only did we experimentally characterize the skirt-like annular wetting ridge but also developed a geometry-inspired simple-to-use semianalytical model that captures important features of the wetting ridge. We validated the model using experiments and Surface Evolver. For this study, we used glass slides that are coated with nano-colloids followed by silicone oil infusion. The insights presented in this work improve the current understanding in the field.

2. MATERIALS AND METHODS

2.1. Theoretical Background. Growth of the wetting ridge around droplets deposited on soft matter is a subject matter in several studies.[45−47] The principal reason for wetting ridge formation and growth on soft matter and/or textured lubricant-infused surfaces is the imbalance of interfacial forces at the contact line. On solid substrates (for example, a copper plate), the vertical component of the surface tension force is not strong enough to deform the substrate. In soft matter (for example, silicone gel), however, the vertical component of the surface tension force can deform the material to some degree. On lubricant-infused hemi-solid hemi-liquid surface, the unbalanced surface tension force causes lubricant transport near the droplet base. The net interfacial force siphons oil from the surrounding and accumulates it near the droplet base, forming a skirt-like annular wetting ridge. As shown in Figure 1, the water−air interfacial tension (γ_{wa}) pulls the contact line upward while the oil−air (γ_{oa}) and oil−water (γ_{ow}) interfacial forces counteract this upward pull. This force balance at the contact line determines the presence or absence of a cloaking layer.[48,49] Importantly, this imbalance of forces continues to pull lubricant from the surroundings via capillary action that leads to wetting ridge formation and growth. This feature is attributed to the self-healing behavior of such surfaces after mechanical damage. The force balance at the contact line that gives rise to a meniscus that is curved inward (and hence negative pressure compared to ambient pressure) is shown schematically in Figure 1.

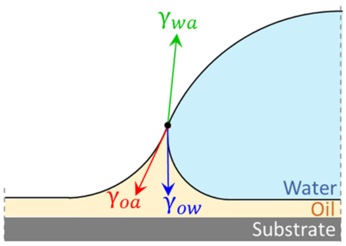

Figure 1. Schematic wetting ridge. Force balance at the contact line where the lubricant oil, water, and air meet determines whether the lubricant oil wraps around the droplet. Owing to the concave inward meniscus shape of the oil−air interface, the region near the droplet base is at lower pressure than the ambient pressure. This low-pressure region siphons oil radially inward from the surrounding oil-infused textured surface. The accumulation of oil near the droplet base gives rise to a skirt-like annular wetting ridge. Depending on oil availability, the wetting ridge can grow and become comparable with the droplet volume.

2.2. Sample Fabrication. The test samples used for this study were fabricated from standard microscope glass slides coated with superhydrophobic nano-colloids. During sample preparation, the test samples were wet cleaned using ethanol, isopropanol alcohol, and deionized water followed by air drying using compressed nitrogen gas. The samples were then plasma-treated in a nitrogen environment for 15 min. Following the plasma cleaning procedure, the samples were hydrophobized by coating them with methanol-diluted nano-colloidal particles. Finally, the nano-textured hydrophobized samples were overlubricated with silicone oil by applying excess lubricant oil. After securely attaching the sample by pulling a vacuum on a spin coater, the overlubricated glass slide was rotated at a specified spin rate (revolutions per minute, rpm) and spin duration to get the desired lubricant film thickness. The schematic of the sample preparation and lubricant coating protocol is shown in Figure 2. In a typical experiment, we used a surface coated with ≈25 μm lubricant oil. For all experiments, we used a 10 μl water droplet that is gently placed on the lubricant-infused surface using a micropipette. A full description of the sample fabrication protocol with scanning electron microscopy (SEM) images is provided in Supporting Information S1.

2.3. Data Collection. All of our experiments were conducted in a laboratory environment (≈23 °C and ≈50% relative humidity) on a goniometer (DSA100E, KRÜSS GmbH). In a typical experiment, a water droplet was deposited gently on a silicone oil-infused glass slide. Irrespective of the oil viscosity, the droplet (≈10 μl) forms an annular skirt-like wetting ridge as shown in Figure 3a. Images of the droplet were recorded using the built-in camera of the goniometer. The time-lapse images were converted into gray scale for edge detection in Matlab, which gives the contour of the droplet and wetting ridge as shown in Figure 3b. Due to the low Bond number (Bo ≈ 0.25), which compares inertia with surface tension, the droplets were nearly hemispherical featuring an apparent contact angle of ≈90° as discussed in detail in Supporting Information S2. Bond number is given by $Bo = \rho g R^2/\gamma$, where ρ is density, g is gravity, R is drop radius, and γ is the surface tension of the droplet. Consequently, both the droplet and the wetting ridge were approximated by fitting circles along the liquid−air interface, as shown in Figure 3c. The detailed procedure for droplet shape analysis is discussed in Supporting Information S3. A schematic depiction of the droplet on the nano-textured lubricant-infused surface is shown in Figure 3d with the droplet, wetting ridge, and droplet base radii denoted as R_d, R_{wr}, and R_Q, respectively, while the height of the wetting ridge is denoted as h_{wr}. The droplet base radius (R_Q) is estimated by selecting the midpoint of the oil meniscus as shown in Figure 3d. The intersection of the wetting ridge with the droplet is used to determine the wetting ridge height h_{wr}. Diffusion-induced droplet evaporation was minimized by enclosing the droplet using an optically transparent glass cuvette. The wetting ridge growth dynamics was captured by acquiring images at 10 frames-per-second (fps). The Matlab processed droplet image used to deduce R_d, R_{wr}, R_Q, and h_{wr} is shown in Figure 3e. The height of the wetting ridge is determined by identifying the intersection point of the circles fitting the droplet and the wetting ridge.

3. RESULTS

3.1. Experiments. We analyzed the time-lapse images to obtain the height of the wetting ridge (h_{wr}), the radius of the wetting ridge (R_{wr}), and the droplet base radius (R_Q). Results show that the wetting ridge (R_{wr}) grows relatively fast initially as shown by the red line in Figure 4a. The growth rate slows down after 30 min and the wetting ridge radius approaches the droplet extended base radius (R_Q) asymptotically while the droplet radius remain nearly constant (R_d). This result shows the effectiveness of our strategy in suppressing droplet evaporation by covering it using the glass cuvette. Similarly, the height of the wetting ridge grows quickly initially and reached steady state after ≈20 min, as shown in Figure 4b. In our experiments, we observed that the time required to reach steady state is a strong function of the lubricant viscosity, a point that will be discussed in a later paragraph.

https://doi.org/10.1021/acsami.4c20298
ACS Appl. Mater. Interfaces 2025, 17, 31677−31684

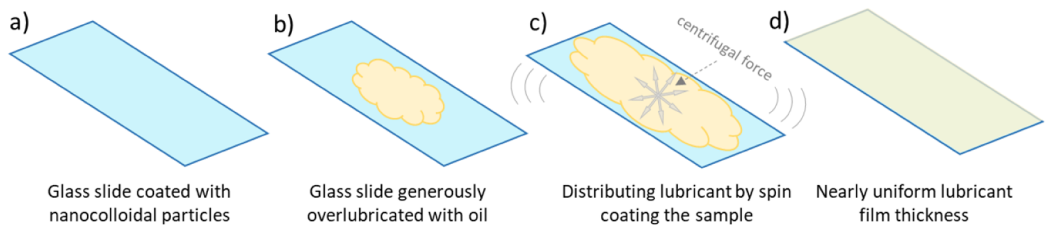

Figure 2. Test sample fabrication protocol. a) A microscope glass slide was coated with hydrophobic colloidal nanoparticles. b) The nano-colloid coated glass slide was over lubricated with silicone oil. c) The glass slide was firmly secured on a spin coater by pulling vacuum. The rotational speed and duration were varied to achieve the desired lubricant film thickness. d) The excess oil on the textured glass slide was thrown out from the surface due to centrifugal force during spin coating. Capillarity force is attributed to immobilizing the lubricant film on the nano-textured glass slide.

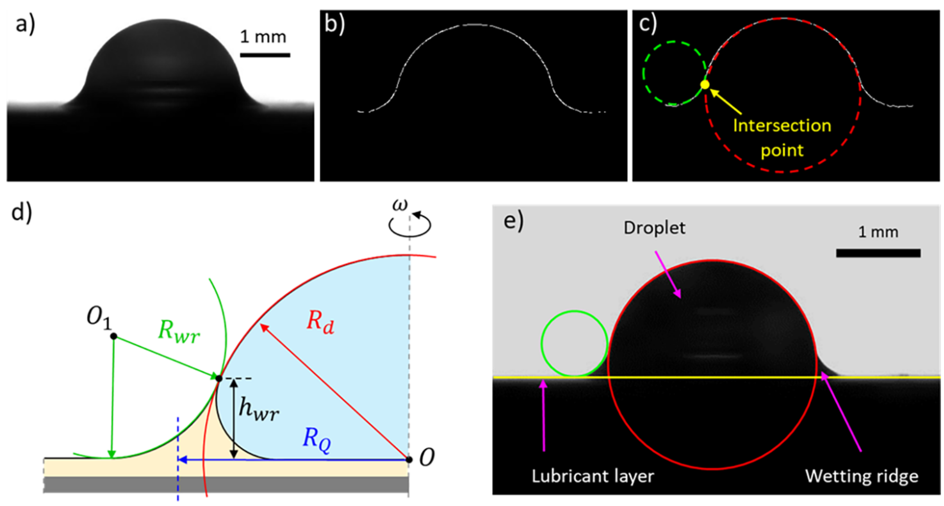

Figure 3. Wetting ridge. a) Image of a water droplet residing on a textured surface infused with silicone oil (10 cSt at 20 °C) a few seconds after deposition (scale bar = 1 mm). b) Camera image converted to binary using edge detection in Matlab. c) Droplet and wetting ridge fitted with circles. d) Schematic of the water droplet (center "O") on the lubricant-infused surface. The respective droplet radius, wetting ridge radius (center "O_1"), and droplet base radius are denoted as R_d, R_{wr}, and R_Q while the height of the wetting ridge is denoted as h_{wr}. e) The droplet image after being processed for curve fitting using a custom Matlab script.

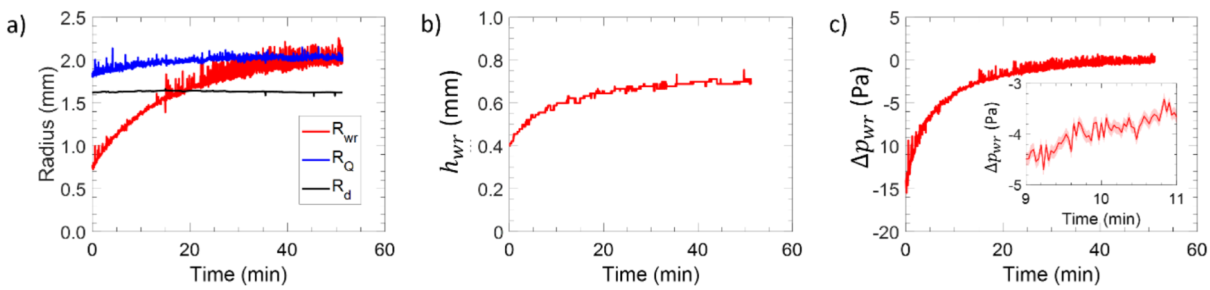

Figure 4. Wetting ridge growth rate. a) Growth rate of the three radii (R_d, R_Q, and R_{wr}). The droplet radius R_d is nearly constant while the wetting ridge R_{wr} and droplet base radius R_Q converge toward each other with time. Droplet radius (R_d) is maintained nearly constant by enclosing the droplet in an optically transparent glass cuvette that suppresses diffusion-driven droplet evaporation. b) Wetting ridge height (h_{wr}) as a function of time obtained from analyzing time-lapse images. c) Pressure deficit of the wetting ridge (Δp_{wr}), which is given by subtracting ambient pressure (p_{amb}) from the wetting ridge pressure (p_{wr}) using $\Delta p_{wr} = p_{wr} - p_{amb}$. Negative pressure indicates pressure below ambient. The inset shows the pressure measurement from meniscus curvature 9 min after deposition with a 95% confidence interval.

We rationalize these results by looking at the pressure in the wetting ridge. Owing to its inward curvature (concave inwards), the pressure in the wetting ridge is below ambient ($p_{amb} \approx 1$ atm) and this difference is denoted using Δp_{wr}. The ambient and wetting ridge pressures are related through the classical Young–Laplace equation,[19] which is given by $p_{wr} = p_{amb} + \gamma_{oa}\ (1/R_{wr} + 1/R_Q)$, where γ_{oa} is the surface tension of the lubricant oil ($\gamma_{oa} \approx 18.57$ dyn/cm),[49] and R_{wr} and R_Q are the two principal radii of curvature of the oil menisci near the droplet base. The steady-state wetting ridge growth rate corresponds to a near zero pressure difference with ambient air pressure as shown in Figure 4c. The inset shows the pressure measurement from meniscus curvature with 95% confidence interval between 9 and 11 min after initial deposition. This pressure difference is given by $\Delta p_{wr} = p_{wr} - p_{amb} = \gamma_{oa}(1/R_{wr} + 1/R_Q)$. Our experimental results suggest that the two principal radii of curvature are equal in magnitude and opposite in direction since $1/R_{wr} + 1/R_Q = 0$. This analysis shows that at steady-state, $|R_{wr}| \approx |R_Q|$, a result that will be further validated using Surface Evolver numerical simulations.

https://doi.org/10.1021/acsami.4c20298
ACS Appl. Mater. Interfaces 2025, 17, 31677−31684

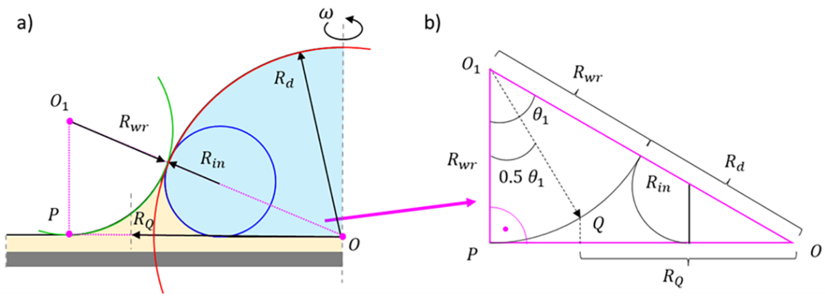

Figure 5. Wetting ridge model. a) Schematic of a water droplet residing on a textured lubricant-infused surface. The droplet and wetting ridge radii are represented by R_d and R_{wr}, respectively. A smaller circle with a radius R_{in} is used to accurately capture the shape of the droplet near its base. b) Geometrical representation of the right angle that forms by connecting the center of the droplet (O), center of the wetting ridge (O_1), and merging point of the wetting ridge with the lubricant film (P). The line connecting O and O_1 passes through the intersection of the wetting ridge with the droplet, which is used to define the wetting ridge height. This geometrical depiction is developed to capture the steady-state wetting ridge shape.

3.2. Analytical Modeling. In our experiments, we observed that the wetting ridge grows steadily until its radius approaches the droplet radius. Water droplets residing on nano-textured silicone oil-infused surfaces are nearly hemispherical[50,51] with a ≈90° contact angle (see Supporting Information S2). We used this understanding as a foundation for our analytical model. Note that this model is valid for sessile droplets with Bond number below 0.25. As shown schematically in Figure 5a, we approximate the inside and outside of the wetting ridge and the droplet using circles. Connecting P, O, and O_1 (Figure 5a) gives a right triangle with legs PO and PO_1 and a hypotenuse OO_1 as shown in Figure 5b. In our schematic, $PO_1 \approx R_{wr}$ and $OO_1 \approx R_d + R_{wr}$, where R_d and R_{wr} are the radii of the droplet and wetting ridge, respectively. These dimensions are related through a simple trigonometric relations using the equation

$$\cos\theta_1 = \frac{R_{wr}}{R_{wr} + R_d} = \frac{R_{wr} - R_{in}}{R_{wr} + R_{in}} \tag{1}$$

where θ_1 is the angle between OO_1 and O_1P and R_{in} is the inner radius of the wetting ridge from the droplet side. The geometric relation in eq 1 can be rearranged to give,

$$R_{in} = \frac{R_{wr}R_d}{2R_{wr} + R_d} \tag{2}$$

Making use of the cosine half-angle trigonometric relation $\cos(\alpha/2) = \sqrt{0.5 + 0.5\cos(\alpha)}$, eq 1 can be rewritten in a simpler form using

$$\cos(\theta_1/2) = \sqrt{\frac{R_d + R_{wr}}{2(R_{wr} + R_d)}} \tag{3}$$

Similarly, we can use sine half-angle function to show

$$\sin(\theta_1/2) = \sqrt{\frac{R_d}{2(R_{wr} + R_d)}} \tag{4}$$

Zero pressure in the wetting ridge at steady-state implies $|R_{wr}| = |R_Q|$. The Pythagoras theorem shown in eq 4, that is $|PO|^2 + |O_1P|^2 = |O_1O|^2$, written in terms of the different radii is given by,

$$(R_Q + R_{wr}\sin(\theta_1/2))^2 + R_{wr}{}^2 = (R_{wr} + R_d)^2 \tag{5}$$

Equation 5 can be rearranged to give the wetting ridge radius as,

$$|R_{wr}| = |R_Q| = \sqrt{(R_d + R_{wr})^2 - R_{wr}{}^2} - R_{wr}\sin(\theta_1/2) \tag{6}$$

Further simplification of the wetting ridge expression in eq 6 gives an implicit solution for the wetting ridge radius (R_{wr}) as

$$R_{wr} = \mp\left(\sqrt{R_d^2 + 2R_{wr}R_d} - R_{wr}\sqrt{\frac{R_d}{2(R_{wr} + R_d)}}\right) \tag{7}$$

where the "∓" comes from solving the quadratic equation shown in eq 5. The only positive root of eq 7 is $R_{wr} = 1.30R_d$ at steady-state, with corresponding values of the cosine angle $\cos(\theta_1) = 0.56$, which gives $\theta_1 = 56°$. The height of the wetting ridge h_{wr} can then be derived as the height of the intersection point of the wetting ridge and the droplet. Thus, $h_{wr} = R_d\cos(\theta_1) = 0.56R_d$. Substituting these values into eq 1 and rearranging the terms give the wetting ridge radius from the droplet side shown in Figure 5a as $R_{in} = 0.36R_d$.

In order to validate the results from our analytical model, we performed experiments on textured oil-impregnated surfaces. The oil used for impregnation was silicone oil with varying viscosities ranging from 5 to 15 cSt. We analyzed the time-lapse images of the droplet (≈10 μl) to understand the wetting ridge growth rate, in particular, the height of the wetting ridge. A snapshot of the wetting ridge shape at three selected times (t = 0, t = 5, and t = 35 min) for three viscosities is shown in Figure 6a−c. The wetting ridge shape is nearly the same at the initial deposition at t = 0 and after reaching a steady-state growth rate at t = 35 min for all viscosities. However, at t = 5 min, the wetting ridge size scales inversely with oil viscosity, that is, the wetting ridge has the largest radius for 5 cSt (orange, Figure 6b) followed by 10 cSt (green, Figure 6b) and 15 cSt (blue, Figure 6b). Our experiments show that as the oil becomes more viscous, the wetting ridge growth rate decreased. Note that the images of the wetting ridge from the 5, 10, and 15 cSt lubricant oils are superimposed and curve fitted using different colors in Figure 6b for better comparison of the size of the wetting ridge. To show the growth rate, we plotted the wetting ridge height as a function of time in Figure 6d. For all viscosities used in our experiments, the wetting ridge height reached the same steady-state height ≈0.6 mm. However, the time used to reach steady-state varied significantly. As can be seen in Figure 6d, the wetting ridge growth rate reached steady-state 5, 15, and 35 min after initial deposition on the 5, 10, and 15 cSt oils, respectively. The measurement uncertainty, which is attributed mainly to

https://doi.org/10.1021/acsami.4c20298
ACS Appl. Mater. Interfaces 2025, 17, 31677−31684

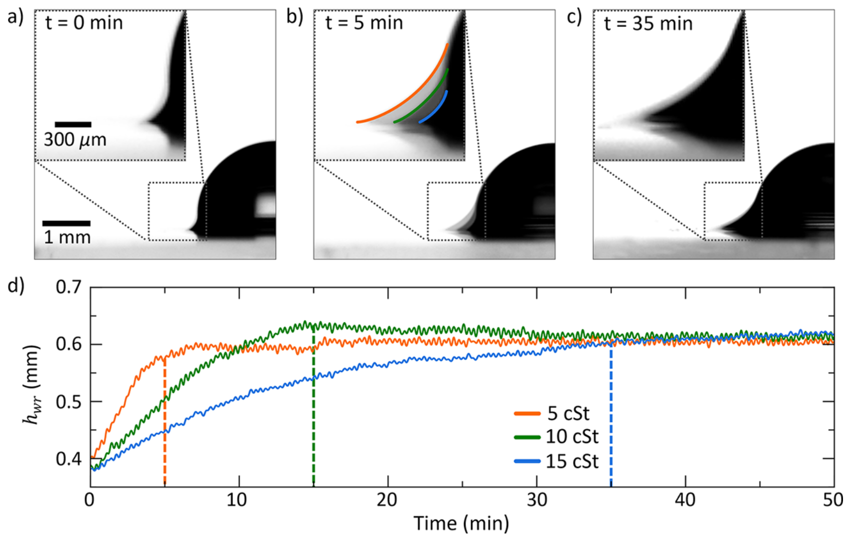

Figure 6. Effect of oil viscosity on wetting ridge growth dynamics. a−c) Sequential images of wetting ridge growth for a water droplet (≈10 μl) on a textured lubricant-infused surface with varying oil viscosity. The wetting ridge growth rate reaches a steady-state after 35 min for all viscosities. As can be seen from the curve fitting, the wetting ridge grows faster for the low-viscosity oil 5 cSt (orange), followed by 10 cSt (green) and 15 cSt (blue). d) Height of the wetting ridge as a function of time. The wetting ridge grows relatively faster initially for all viscosities. Following initial deposition, the wetting ridge growth rate levels off after 5, 15, and 35 min for 5, 10, and 15 cSt oils, respectively. The final steady-state wetting ridge height for all viscosities nearly is the same at ≈0.6 mm. The time to reach steady-state wetting ridge scales inversely with oil viscosity. The uncertainty in our measurement from repeated experiments for one standard deviation is ≈100 μm.

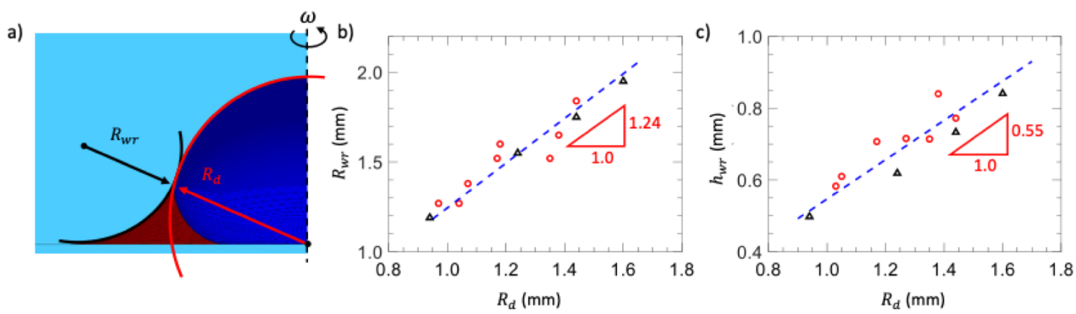

Figure 7. Model validation using Surface Evolver (SE) simulation. a) In the SE numerical simulation, the height of the wetting ridge (h_{wr}) is determined by identifying the intersection point between the wetting ridge and the water droplet. b) Wetting ridge radius (R_{wr}) as a function of the droplet radius (R_d). c) Wetting ridge height (h_{wr}) as a function of the droplet radius. The red circles are experimental data while the black triangles are obtained from SE simulation. This result shows that $R_{wr} = 1.24R_d$ and $h_{wr} = 0.55R_d$, a result that agrees well with our analytical model that gives $R_{wr} = 1.30R_d$ and $h_{wr} = 0.56R_d$. The measurement uncertainty from repeated experiments for one standard deviation is ≈100 μm. The error bars are smaller than the data points.

repeated measurements for one standard deviation, in our experiments is ≈100 μm.

3.3. Numerical Validation. To validate our model, we simulated a wetting ridge numerically using Surface Evolver (SE). For numerical simulation, we set the different interfacial tensions (water−air, oil−air, and water−oil) based on our prior work, which measured these interfacial forces experimentally using the coventional pendant droplet method.[49,52] By changing the volume of the water droplet, we obtained different droplet radii and compared the relationship between the radius and height of the wetting ridge. The geometrical quantities R_{wr}, R_d, and h_{wr} are estimated from the cross-section image shown in Figure 7a. As shown in Figure 7b,c, the wetting ridge radius scales linearly with droplet radius R_d with slope 1.24, a result that agrees with our geometry-based analytical model, which gives a 1.3 prefactor in eq 8. Similarly, the wetting ridge height h_{wr} scales linearly with R_d with a slope of 0.55 slope, a result that matches well with our analytical model, which gives 0.56 in eq 8. The red circles in Figure 7b,c are experimental data while the black triangles are obtained from SE simulation. The good agreement between our experiments and the SE simulation further validates our geometry-based analytical wetting ridge model.

3.4. Steady-State Wetting Ridge Volume. After validating our geometry-based analytical wetting ridge model with both experiments and the Surface Evolver simulation, we used it to estimate the volume of the lubricant oil that accumulates near the droplet base. Due to axial symmetry, we used only half of the droplet and the skirt-like wetting ridge for schematic depiction in Figure 8a. First, we cut through the droplet and wetting ridge at the droplet's center. The cross-sectional area of the wetting ridge at this midsection is represented by the blue hatched section in Figure 8b. Using purely geometric arguments, the area of the hatched section is given by,

https://doi.org/10.1021/acsami.4c20298
ACS Appl. Mater. Interfaces 2025, 17, 31677−31684

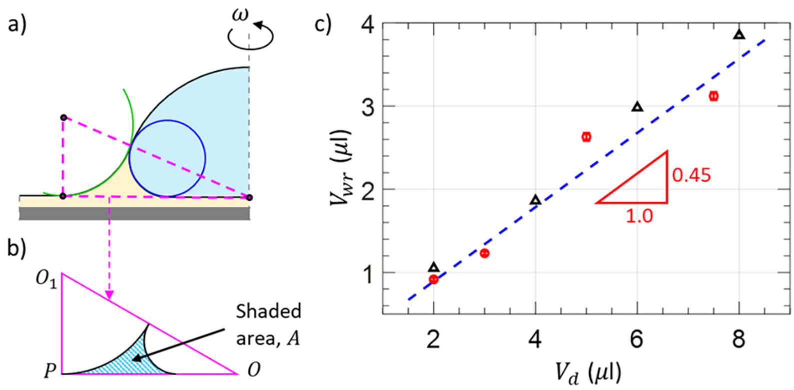

Figure 8. Wetting ridge volume. a) Schematic of the droplet and wetting ridge. b) Cross sectional area of the wetting ridge near the droplet base. The wetting ridge is represented by the blue hatched region. c) Volume of the wetting ridge as a function of the droplet volume. The wetting ridge volume is obtained by rotating the cross sectional area A (blue hatched area) along the axis of the droplet. The red hollow circles are experimental data points while the black hollow triangles are Surface Evolver simulation results. At steady-state, the wetting ridge volume is ≈50% of the droplet volume. The measurement uncertainty is <0.1 μl. The error bars are smaller than the data points.

$$A = \frac{1}{2}R_{wr}^2 \tan\theta_1 - \frac{\theta_1}{2}R_{wr}^2 - \left(\frac{1}{2}R_{in}^2 \tan\theta_1 + \frac{\pi - \theta_1}{2}R_{in}^2\right) \tag{8}$$

where A is the cross-sectional area of the wetting ridge at the midplane. This cross-sectional area is rotated along the droplet axis (ω, Figure 8a) to estimate the wetting ridge volume V_{wr}. The details of the numerical integration of the wetting ridge volume using Matlab is given in Supporting Information S3. Comparing the wetting ridge volume V_{wr} against the droplet volume V_d shows that at steady-state the wetting ridge volume is nearly half (≈50%) of the droplet volume as can be seen from the 0.45 prefactor when plotting the wetting ridge volume (V_{wr}) against the droplet volume (V_d). The red hollow circles are obtained experimentally while the black hollow triangles are obtained using Surface Evolver simulation.

4. SUMMARY

This study investigates the transient behavior and steady-state shape of the skirt-like annular wetting ridge that forms when a water droplet is deposited on a micro/nanotextured lubricant-infused surface. The root cause of the wetting ridge is the imbalance of interfacial forces at the contact line. A geometry-based analytical model reveals that the axisymmetric concave meniscus creates a low-pressure region near the droplet base that is credited for siphoning oil from the surrounding. This dynamics at the contact line gives rise to the transient nature of the skirt-like annular wetting ridge. The growth rate of the wetting ridge slows down and reaches steady-state when the wetting ridge pressure equilibrates with ambient pressure. Additionally, our analytical model that is validated using experiments and surface evolver simulation shows that at steady-state (1) the two principal radii of the annular wetting ridge are equal in magnitude and opposite in direction (that is, one principal radius lies inside the wetting ridge on the liquid side while the other principal radius lies outside the wetting ridge on the air side), (2) the gauge pressure inside the wetting ridge is zero, (3) the wetting ridge radius is ≈30% larger than the droplet radius, (4) the wetting ridge height is ≈50% of the droplet radius, and (5) the wetting ridge volume is ≈50% of the droplet volume. Moreover, our experiments show that the steady-state wetting ridge shape is insensitive to the oil viscosity used for impregnation. The time to reach steady-state, however, scales inversely with the lubricant viscosity. Our results show that the primary driving force for wetting ridge growth is the unbalanced vertical component of surface tension force at the contact line. The geometry-inspired and simple-to-use wetting ridge model presented in this study provides useful insights into wetting ridge growth dynamics and its steady-state nature. Besides improving the current state-of-the-art understanding of the origin and growth dynamics of the skirt-like annular wetting ridge, the useful insights gained from this work inform strategies and practical avenues to manipulate wetting ridge growth, a result that has implications in lubricant depletion mitigating strategies. Note that currently, wetting ridge is believed to have a major contribution to oil depletion, a concern that has hindered the adoption of these lubricant-infused surfaces for industrial application.

ASSOCIATED CONTENT

Supporting Information

The Supporting Information is available free of charge at https://pubs.acs.org/doi/10.1021/acsami.4c20298.

Details of sample preparation, droplet shape analysis, image processing, and wetting ridge volume modeling (PDF)

AUTHOR INFORMATION

Corresponding Author

Solomon Adera − *Energy Transport Lab, Department of Mechanical Engineering, University of Michigan, Ann Arbor, Michigan 48109, United States;* orcid.org/0000-0002-3249-301X; Email: sadera@umich.edu

Authors

Haobo Xu − *Energy Transport Lab, Department of Mechanical Engineering, University of Michigan, Ann Arbor, Michigan 48109, United States;* orcid.org/0009-0002-3011-9291

Tomasz Kulakowski − *Energy Transport Lab, Department of Mechanical Engineering, University of Michigan, Ann Arbor, Michigan 48109, United States; Faculty of Civil Engineering, Warsaw University of Technology, Warsaw 00-661, Poland;* orcid.org/0000-0001-7713-9156

https://doi.org/10.1021/acsami.4c20298
ACS Appl. Mater. Interfaces 2025, 17, 31677−31684

Young Jin Lee − *Energy Transport Lab, Department of Mechanical Engineering, University of Michigan, Ann Arbor, Michigan 48109, United States;* orcid.org/0000-0002-1396-7355

Complete contact information is available at: https://pubs.acs.org/10.1021/acsami.4c20298

Author Contributions

[§]H.X. and T.K. contributed equally. All authors contributed to writing and agreed on the final version.

Funding

This work was supported by the National Science Foundation (Award Number CBET-2427827).

Notes

The authors declare no competing financial interest.

REFERENCES

(1) Adera, S.; Alvarenga, J.; Shneidman, A. V.; Zhang, C. T.; Davitt, A.; Aizenberg, J. Depletion of Lubricant from Nanostructured Oil-Infused Surfaces by Pendant Condensate Droplets. *ACS Nano* **2020**, *14* (7), 8024−8035.

(2) Miljkovic, N.; Enright, R.; Wang, E. N. Modeling and Optimization of Superhydrophobic Condensation. *J. Heat Transfer.* **2013**, *135* (11), 111004−111027.

(3) Xiao, R.; Miljkovic, N.; Enright, R.; Wang, E. N. Immersion condensation on oil-infused heterogeneous surfaces for enhanced heat transfer. *Sci. Rep.* **2013**, *3*, 1988.

(4) Xie, J.; Xu, J. L.; Li, X.; Liu, H. Dropwise condensation on superhydrophobic nanostructure surface, Part I: Long-term operation and nanostructure failure. *Int. J. Heat Mass Transfer.* **2019**, *129*, 86−95.

(5) Adera, S.; Naworski, L.; Davitt, A.; Mandsberg, N. K.; Shneidman, A. V.; Alvarenga, J.; Aizenberg, J. Enhanced condensation heat transfer using porous silica inverse opal coatings on copper tubes. *Sci. Rep.* **2021**, *11* (1), 10675.

(6) Zhou, Y.; Adera, S. Boiling limit on textured oil-impregnated surfaces*InterPACK 2023, San Diego, California, October 24−26, 2023*; ASME: San Diego, California, 2023, DOI: 10.1115/IPACK2023-111736.

(7) Song, Y.; Gong, S.; Vaartstra, G.; Wang, E. N. Microtube Surfaces for the Simultaneous Enhancement of Efficiency and Critical Heat Flux during Pool Boiling. *ACS Appl. Mater. Interfaces* **2021**, *13* (10), 12629−12635.

(8) Song, Y.; Jiang, S.; Li, G.; Zhang, Y.; Wu, H.; Xue, C.; You, H.; Zhang, D.; Cai, Y.; Zhu, J. Cross-Species Bioinspired Anisotropic Surfaces for Active Droplet Transportation Driven by Unidirectional Microcolumn Waves. *ACS Appl. Mater. Interfaces* **2020**, *12* (37), 42264−42273.

(9) Antao, D. S.; Adera, S.; Zhu, Y.; Farias, E.; Raj, R.; Wang, E. N. Dynamic Evolution of the Evaporating Liquid-Vapor Interface in Micropillar Arrays. *Langmuir* **2016**, *32* (2), 519−526.

(10) Adera, S.; Antao, D. S.; Raj, R.; Wang, E. N. Hotspot Thermal Management via Thin-Film Evaporation—Part I: Experimental Characterization. *IEEE Trans. Compon., Packag. Manuf. Technol.* **2018**, *8* (1), 88−98.

(11) Somasundaram, S.; Zhu, Y.; Lu, Z.; Adera, S.; Bin, H.; Mengyao, W.; Tan, C. S.; Wang, E. N. Thermal design optimization of evaporator micropillar wicks. *Int. J. Therm. Sci.* **2018**, *134*, 179−187.

(12) Lu, H.; Shi, W.; Guo, Y.; Guan, W.; Lei, C.; Yu, G. Materials Engineering for Atmospheric Water Harvesting: Progress and Perspectives. *Adv. Mater.* **2022**, *34* (12), No. e2110079.

(13) Dai, X.; Sun, N.; Nielsen, S. O.; Stogin, B. B.; Wang, J.; Yang, S.; Wong, T. S. Hydrophilic directional slippery rough surfaces for water harvesting. *Sci. Adv.* **2018**, *4* (3), No. eaaq0919.

(14) Wang, L.; Yin, K.; Deng, Q.; Huang, Q.; He, J.; Duan, J. A. Wetting Ridge-Guided Directional Water Self-Transport. *Adv. Sci.* **2022**, *9* (34), No. e2204891.

(15) Solomon, B. R.; Khalil, K. S.; Varanasi, K. K. Drag reduction using lubricant-impregnated surfaces in viscous laminar flow. *Langmuir* **2014**, *30* (36), 10970−10976.

(16) Kolle, S.; Davitt, A.; Zhou, Y.; Aizenberg, J.; Adera, S. Synergistic Benefits of Micro/Nanostructured Oil-Impregnated Surfaces in Reducing Fouling while Enhancing Heat Transfer. *Langmuir* **2023**, *39* (19), 6705−6712.

(17) Lin, M.; Kim, P.; Arunachalam, S.; Hardian, R.; Adera, S.; Aizenberg, J.; Yao, X.; Daniel, D. Emergent Collective Motion of Self-Propelled Condensate Droplets. *Phys. Rev. Lett.* **2024**, *132* (5), 058203.

(18) Quéré, D. Wetting and Roughness. *Annu. Rev. Mater. Res.* **2008**, *38* (1), 71−99.

(19) Gennes, P.-G.; Brochard-Wyart, F.; Quéré, D. *Capillarity and wetting phenomena: drops, bubbles, pearls, waves*; Springer: New York, NY, 2004.

(20) Joanny, J. F.; de Gennes, P. G. A model for contact angle hysteresis. *J. Chem. Phys.* **1984**, *81* (1), 552−562.

(21) Eral, H. B.; 't Mannetje, D. J. C. M.; Oh, J. M. Contact angle hysteresis: a review of fundamentals and applications. *Colloid Polym. Sci.* **2013**, *291* (2), 247−260.

(22) Park, K. C.; Kim, P.; Grinthal, A.; He, N.; Fox, D.; Weaver, J. C.; Aizenberg, J. Condensation on slippery asymmetric bumps. *Nature* **2016**, *531* (7592), 78−82.

(23) Bohn, H. F.; Federle, W. Insect aquaplaning: Nepenthes pitcher plants capture prey with the peristome, a fully wettable water-lubricated anisotropic surface. *Proc. Natl. Acad. Sci. U. S. A.* **2004**, *101* (39), 14138−14143.

(24) Bauer, U.; Bohn, H. F.; Federle, W. Harmless nectar source or deadly trap: Nepenthes pitchers are activated by rain, condensation and nectar. *Proc. Biol. Sci.* **2008**, *275*, 259−265.

(25) Bauer, U.; Di Giusto, B.; Skepper, J.; Grafe, T. U.; Federle, W. With a flick of the lid: a novel trapping mechanism in Nepenthes gracilis pitcher plants. *PLoS One* **2012**, *7* (6), No. e38951.

(26) Bauer, U.; Paulin, M.; Robert, D.; Sutton, G. P. Mechanism for rapid passive-dynamic prey capture in a pitcher plant. *Proc. Natl. Acad. Sci. U. S. A.* **2015**, *112* (43), 13384−13389.

(27) Scholz, I.; Buckins, M.; Dolge, L.; Erlinghagen, T.; Weth, A.; Hischen, F.; Mayer, J.; Hoffmann, S.; Riederer, M.; Riedel, M.; Baumgartner, W. Slippery surfaces of pitcher plants: Nepenthes wax crystals minimize insect attachment via microscopic surface roughness. *J. Exp. Biol.* **2010**, *213* (7), 1115−1125.

(28) Quéré, D. Non-sticking drops. *Rep. Prog. Phys.* **2005**, *68* (11), 2495−2532.

(29) Wong, T. S.; Kang, S. H.; Tang, S. K.; Smythe, E. J.; Hatton, B. D.; Grinthal, A.; Aizenberg, J. Bioinspired self-repairing slippery surfaces with pressure-stable omniphobicity. *Nature* **2011**, *477* (7365), 443−447.

(30) Lafuma, A.; Quéré, D. Slippery pre-suffused surfaces. *Europhys. Lett.* **2011**, *96* (5), 56001.

(31) Smith, J. D.; Dhiman, R.; Anand, S.; Reza-Garduno, E.; Cohen, R. E.; McKinley, G. H.; Varanasi, K. K. Droplet mobility on lubricant-impregnated surfaces. *Soft Matter* **2013**, *9* (6), 1772−1780.

(32) Epstein, A. K.; Wong, T. S.; Belisle, R. A.; Boggs, E. M.; Aizenberg, J. Liquid-infused structured surfaces with exceptional anti-biofouling performance. *Proc. Natl. Acad. Sci. U. S. A.* **2012**, *109* (33), 13182−13187.

(33) Raj, R.; Enright, R.; Zhu, Y.; Adera, S.; Wang, E. N. Unified model for contact angle hysteresis on heterogeneous and super-hydrophobic surfaces. *Langmuir* **2012**, *28* (45), 15777−15788.

(34) Adera, S.; Antao, D.; Raj, R.; Wang, E. N. Design of micropillar wicks for thin-film evaporation. *Int. J. Heat Mass Transfer.* **2016**, *101*, 280−294.

(35) Raj, R.; Adera, S.; Enright, R.; Wang, E. N. Polygonal Droplets on Microstructured Surfaces. *J. Heat Transfer.* **2014**, *136* (8), 080906.

(36) Keiser, A.; Keiser, L.; Clanet, C.; Quere, D. Drop friction on liquid-infused materials. *Soft Matter* **2017**, *13* (39), 6981−6987.
(37) Keiser, A.; Baumli, P.; Vollmer, D.; Quéré, D. Universality of friction laws on liquid-infused materials. *Phys. Rev. Fluids* **2020**, *5* (1), 014005.
(38) Rotenberg, Y.; Boruvka, L.; Neumann, A. W. Determination of Surface Tension and Contact Angle from the Shapes of Axisymmetric Fluid Interfaces. *J. Colloid Interface Sci.* **1983**, *93* (1), 169−183.
(39) Cabezas, M. G.; Bateni, A.; Montanero, J. M.; Neumann, A. W. Determination of surface tension and contact angle from the shapes of axisymmetric fluid interfaces without use of apex coordinates. *Langmuir* **2006**, *22* (24), 10053−10060.
(40) Marchand, A.; Das, S.; Snoeijer, J. H.; Andreotti, B. Contact angles on a soft solid: from Young's law to Neumann's law. *Phys. Rev. Lett.* **2012**, *109* (23), 236101.
(41) Gunjan, M. R.; Kumar, A.; Raj, R. Cloaked Droplets on Lubricant-Infused Surfaces: Union of Constant Mean Curvature Interfaces Dictated by Thin-Film Tension. *Langmuir* **2021**, *37* (22), 6601−6612.
(42) Dai, Z.; Vella, D. Droplets on lubricated surfaces: The slow dynamics of skirt formation. *Phys. Rev. Fluids* **2022**, *7* (5), 054003.
(43) Schellenberger, F.; Xie, J.; Encinas, N.; Hardy, A.; Klapper, M.; Papadopoulos, P.; Butt, H. J.; Vollmer, D. Direct observation of drops on slippery lubricant-infused surfaces. *Soft Matter* **2015**, *11* (38), 7617−7626.
(44) Sadullah, M. S.; Semprebon, C.; Kusumaatmaja, H. Drop Dynamics on Liquid-Infused Surfaces: The Role of the Lubricant Ridge. *Langmuir* **2018**, *34* (27), 8112−8118.
(45) Roy, R.; Seiler, R. L.; Weibel, J. A.; Garimella, S. V. Droplets on Soft Surfaces Exhibit a Reluctance to Coalesce due to an Intervening Wetting Ridge. *Adv. Mater. Interfaces* **2020**, *7* (17), 2000731.
(46) Park, S. J.; Weon, B. M.; Lee, J. S.; Lee, J.; Kim, J.; Je, J. H. Visualization of asymmetric wetting ridges on soft solids with X-ray microscopy. *Nat. Commun.* **2014**, *5*, 4369.
(47) Gerber, J.; Lendenmann, T.; Eghlidi, H.; Schutzius, T. M.; Poulikakos, D. Wetting transitions in droplet drying on soft materials. *Nat. Commun.* **2019**, *10* (1), 4776.
(48) Xu, H.; Herzog, J. M.; Zhou, Y.; Bashirzadeh, Y.; Liu, A.; Adera, S. Visualization and Experimental Characterization of Wrapping Layer Using Planar Laser-Induced Fluorescence. *ACS Nano* **2024**, *18* (5), 4068−4076.
(49) Gandee, H.; Zhou, Y.; Lee, J.; Chomali, J.; Xu, H.; Adera, S. Unique ice dendrite morphology on state-of-the-art oil-impregnated surfaces. *Proc. Natl. Acad. Sci. U. S. A.* **2023**, *120* (1), No. e2214143120.
(50) Barrio-Zhang, H.; Ruiz-Gutierrez, E.; Armstrong, S.; McHale, G.; Wells, G. G.; Ledesma-Aguilar, R. Contact-Angle Hysteresis and Contact-Line Friction on Slippery Liquid-like Surfaces. *Langmuir* **2020**, *36* (49), 15094−15101.
(51) McHale, G.; Orme, B. V.; Wells, G. G.; Ledesma-Aguilar, R. Apparent Contact Angles on Lubricant-Impregnated Surfaces/SLIPS: From Superhydrophobicity to Electrowetting. *Langmuir* **2019**, *35* (11), 4197−4204.
(52) Xu, H.; Zhou, Y.; Daniel, D.; Herzog, J.; Wang, X.; Sick, V.; Adera, S. Droplet attraction and coalescence mechanism on textured oil-impregnated surfaces. *Nat. Commun.* **2023**, *14* (1), 4901.